Journal of The Electrochemical Society, 2021 **168** 034519

The Impact of Sintering Atmosphere and Temperature on the Phase Evolution of High Surface Area LSCF Prepared by In Situ Carbon Templating

Sixbert P. Muhoza,[1,2,3] Thomas H. Taylor,[2] Xueyan Song,[1,4] and Michael D. Gross[1,2,3,z]

[1]*United States Department of Energy, National Energy Technology Laboratory, Morgantown, West Virginia, United States of America*
[2]*Department of Engineering, Wake Forest University, Winston-Salem, North Carolina 27101, United States of America*
[3]*Center for Functional Materials, Wake Forest University, Winston-Salem, North Carolina 27101, United States of America*
[4]*Department of Mechanical and Aerospace Engineering West Virginia University, Morgantown, West Virginia 26506, United States of America*

The thermochemical stability of lanthanum strontium cobalt ferrite (LSCF) processed between 1000 °C–1200 °C via the in situ carbon templating method was studied. This method generates high surface area ceramics at traditional solid oxide fuel cell (SOFC) sintering temperatures by generating a carbon template in situ and subsequently removing the template by oxidation at 700 °C. Argon processed samples produced an amorphous carbon template, whereas nitrogen tended to form graphitic carbon. Prior to the oxidation step, nitrogen samples comprised larger La_2O_3 crystallites (22–40 nm) compared to argon (9–17 nm). Upon oxidation, argon samples resulted in a pure LSCF phase with surface areas in the 21–29 $m^2 \cdot g^{-1}$ range, whereas nitrogen samples contained significant impurities. This demonstrates that the size of La_2O_3 crystallites formed during inert processing limited the ability to produce a pure LSCF phase. Symmetrical cells comprising nano-LSCF electrodes generated by the templating method were compared to cells sintered directly in air. Impedance results suggest that nano-LSCF cells and cells processed in air were dominated by interfacial charge transfer resistance and gas diffusion, respectively. The results map out conditions for preparing and integrating high surface area, nanostructured LSCF into SOFC electrodes at traditional sintering temperatures. Strategies for improving the interfacial resistance of nano-LSCF electrodes are discussed.
 [DOI: 10.1149/1945-7111/abf062]

Manuscript submitted February 5, 2021; revised manuscript received March 14, 2021. Published March 30, 2021.

Supplementary material for this article is available online

Lanthanum strontium cobalt ferrite (LSCF) has been extensively studied as a cathode material for intermediate temperature solid oxide fuel cells (IT-SOFC).[1–5] Researchers are interested in the material because of its high electronic and oxide ion conductivity as well as its high oxygen diffusion properties at intermediate temperatures (600 °C–800 °C).[1,6–8] These properties extend reaction sites throughout the cathode, substantially enhancing electrochemical performance.

The most common synthesis methods researched to optimize the conductivity and catalytic properties of LSCF powders are solid-state reaction and wet chemical synthesis methods.[9–15] The solid-state reaction method is attractive because of its low cost and simplicity; however, it requires high temperatures, often resulting in poor compositional homogeneity and low surface area.[9] Hence, researchers have favored preparing LSCF by the wet chemical synthesis methods, which include solution combustion, co-precipitation, sol-gel, and polymeric complexing.[9,11–15] The use of solutions as starting materials ensures homogeneous mixing of precursors at the atomic level and lower calcination temperatures.[9] As a result, many researchers have successfully prepared crystalline LSCF powders with fine and homogeneous particles using wet chemical synthesis methods.[16–19]

While LSCF powders with 100–200 nm particles and crystallites as small as 20 nm have been successfully prepared,[17–19] it has been challenging to make cathodes comprising such small LSCF particles given that SOFCs are sintered at high temperatures (⩾1000 °C). Such high temperatures lead to substantial particle coarsening, which reduces the active site density in electrodes. In our lab, we have developed a processing method that overcomes this challenge. We refer to this novel method as in situ carbon templating, and we have used it to prepare numerous SOFC nanomaterials with particles as small as 10 nm over a broad range of temperatures, 850 °C–1350 °C.[20–25]

The in situ carbon templating method involves two steps. First, a hybrid inorganic-organic material containing precursors of the desired SOFC ceramic is prepared and heated to 850 °C–1350 °C in an inert atmosphere. During this process, an amorphous carbon template forms and surrounds the ceramic nanoparticles, preventing them from coarsening. In the second step, the amorphous carbon is removed by oxidation in air at 700 °C, a temperature which does not cause detrimental coarsening of the nanoparticles.

In a previous study, we have shown the effect of sintering atmosphere on the phase evolution of yttria-stabilized zirconia (YSZ) nanoparticles.[24] It was found that, in some cases, a ZrC impurity phase forms during the high temperature inert processing step, resulting in a monoclinic ZrO_2 impurity phase during the oxidation step. Since monoclinic ZrO_2 is detrimental to the oxide ion conductivity and electrochemical activity of SOFC cathodes,[26–28] it was critical to understand the impact of different sintering atmospheres on impurities and YSZ phase evolution. Under argon, ZrC began to form at 1150 °C; however, ZrC did not form in nitrogen below 1350 °C. It was suggested that nitrogen partially dissoves into YSZ near the surface, suppressing interaction between YSZ and the carbon template.[29–32]

Similarly, we have conducted a systematic study on the thermochemical stability of LSCF under argon and nitrogen atmospheres. Unlike the YSZ results, a pure nano-LSCF (nLSCF) phase was more difficult to produce under a nitrogen atmosphere compared to argon. In the LSCF case, it was determined that the structure of the carbon template and the crystallite size of a La_2O_3 impurity phase could be used to predict whether or not a pure LSCF phase forms. In addition, the electrochemical performance of symmetrical cells comprising nLSCF electrodes was investigated.

[z]E-mail: grossmd@wfu.edu

Experimental

LSCF-Propylene Oxide-Glucose (LSCF-POG) hybrid materials were prepared according to our previously reported procedures.[21–24] First, $La(NO_3)_3{\cdot}6H_2O$ (99.99%, Alfa Aesar), $Sr(NO_3)_2$ (99.0%, Alfa Aesar), $Co(NO_3)_2{\cdot}6H_2O$ (98.0%–102.0%, Alfa Aesar), and $Fe(NO_3)_3{\cdot}9H_2O$ (98+%, Alfa Aesar) were dissolved in deionized water in a La:Sr:Co:Fe:H_2O molar ratio of 3:2:1:4:950. Second, glucose (⩾99.9%, Alfa Aesar) was added to the solution and magnetically stirred until complete dissolution. Samples were prepared with glucose to total metals (Glucose:M) molar ratios between 2.5:1 and 4.5:1 in 0.5:1 increments. Finally, propylene oxide (PO, ⩾99.5%, Sigma-Aldrich) was added to the solution in a PO to total metals (PO:M) molar ratio of 9:1. The resulting solution was heated to 120 °C until a dark brown viscous material formed.

One set of hybrid material samples was sintered under nitrogen (G01 NI300, Arc3, 99.998%) and the other set under argon (G01 AR300, Arc3, 99.997%). In both cases, the gases were flowed at 750 ml·min^{-1}. The temperature was programmed to increase from ambient temperature to 850 °C at 5 °C·min^{-1}, from 850 °C to the sintering temperature at 2 °C·min^{-1}, held at the sintering temperature for 2 h, and then decreased to 850 °C and ambient temperature at 2 °C·min^{-1} and 5 °C·min^{-1}, respectively. Three sintering temperatures were studied: 1000 °C, 1100 °C, and 1200 °C. All samples were subsequently calcined in air at 700 °C for 5 h with a 5 °C·min^{-1} ramp rate. For comparison purposes, LSCF-POG samples with a 4.5:1 Glucose:M molar ratio and commercial LSCF (LSCF-HP, fuelcellmaterials) samples were sintered at 1000 °C, 1100 °C, and 1200 °C in air for 2 h following the same heating schedule.

The concentration of the carbon template generated during the inert processing step was determined via carbon elemental analysis by Complete Analysis Laboratories, Inc. (Parsippany, NJ). The experiments were conducted with a Carlo Erba CHN analyzer by combusting each sample at 1100 °C and quantifying the amount of evolved CO_2 gas. The carbon wt% was then determined from the measured CO_2 amounts. Powder X-ray diffraction (XRD) patterns of both the sintered and calcined samples were collected for phase identification. Patterns were collected with a Bruker D2 Phaser X-ray diffractometer with CuKα radiation, a 2θ range of 20°−60° in 0.02° increments and a 0.3 s time step. The Brunauer, Emmett, Teller (BET) method was used to determine specific surface areas. The BET experiments were conducted with a Micromeritics Tristar II 3020 surface area analyzer with nitrogen adsorption at 77 K. The samples were degassed at 250 °C for 2 h prior to starting the experiments and the correlation coefficients of the reported surface areas were at least 0.9995. Electron diffraction, diffraction contrast, and high-resolution transmission electron microscopy (HRTEM) imaging were performed using a JEM-2100 operated at 200 kV. Chemical analysis was carried out under TEM using energy dispersive X-ray spectroscopy (EDS).

Symmetrical cells comprised of nLSCF electrodes or commercial LSCF (cLSCF) electrodes with a samaria-doped ceria (SDC) electrolyte were prepared as follows. SDC powders (SDC20-TC, fuelcellmaterials) were pressed into pellets and sintered in air at 1400 °C for 5 h. Upon sintering, the diameter and thickness of the pellets were 13.5 mm and 0.6 mm, respectively. LSCF slurries, prepared by mixing either nLSCF or cLSCF with ink vehicle (VEH, fuelcellmaterials) in a 1:1 ratio by weight, were applied on either side of the SDC electrolyte. For nLSCF, the LSCF-POG powder had a 2.5:1 Glucose:M molar ratio and was pre-sintered at 1000 °C in argon. The cLSCF cells were sintered in air while the nLSCF cells were sintered in argon (750 ml·min^{-1}). Both cells were sintered at 1000 °C for 2 h with a 2 °C·min^{-1} ramp rate. The nLSCF cells were subsequently calcined in air at 700 °C for 2 h. For both samples, the effective electrode area was 0.32 cm^2 and the electrodes were ∼20 μm thick.

Symmetrical cell electrochemical performance was investigated with Electrochemical Impedance Spectroscopy (EIS). The experiments were conducted using a potentiostat with four probes (Interface 5000E, Gamry Instruments). Silver paste and silver wires were used for current collection at both electrodes. All tests were conducted in galvanostatic mode with a 0 mA dc current, a 5 mA ac perturbation, and a 10^6 Hz–10^{-1} Hz frequency range. Cells were tested in air at 700 °C, 750 °C, and 800 °C. The resulting impedance spectra were deconvoluted by non-linear least squares regression and the impedance values were divided by two to account for the contribution of the two electrodes.

Results and Discussion

XRD patterns of LSCF-POG treated in nitrogen and subsequently calcined in air are shown in Fig. 1. Upon processing in nitrogen, the primary phases are La_2O_3 and FeCo for all hybrid material formulations. This is expected given that the formation of a carbon template creates a reducing environment and numerous researchers have reported that binary oxide and metal phases are favored over LSCF under low oxygen fugacity atmospheres.[33–35] In general, primary phase peaks become broader with increasing Glucose:M molar ratios, i.e. higher carbon template concentrations, and decreasing processing temperatures. Broader peaks indicate smaller crystallite size, which can be estimated using the Scherrer equation. For example, for a processing temperature of 1200 °C, the crystallite size of La_2O_3 decreases from 39 nm to 27 nm as the Glucose:M molar ratio is increased from 2.5:1 to 4.5:1. In addition, for a Glucose:M molar ratio of 4.5:1, the La_2O_3 crystallite size decreases from 27 nm to 9 nm as the processing temperature is decreased from 1200 °C to 1000 °C. Both trends are consistent with previous studies of YSZ and gadolinium-doped ceria (GDC) derived from hybrid inorganic-organic materials.[23,24]

One feature of the XRD patterns in Fig. 1 that we have not observed in previous studies is the presence of a graphitic carbon peak. A clear graphite peak is observed at a processing temperature of 1200 °C for all Glucose:M molar ratios. For processing temperatures of 1100 °C and 1000 °C, the La_2O_3 peak at a 2θ of 26.1° is too broad to determine whether a graphite peak is present. In Figs. 1a and 1b, one could argue there is a small, broad shoulder on the right side of the La_2O_3 peak for 1100 °C that may be graphite; however, one cannot be certain given the lack of a demarcated peak. Even if graphite was present in these 1100 °C samples, the low intensity and broadness suggests it would be present in low concentration and have a small crystallite size.

In regard to samples treated in nitrogen and then calcined in air, Fig. 1 shows that impurities became more prevalent with increasing processing temperature and decreasing carbon content. For a processing temperature of 1000 °C, the only sample with a significant impurity was the 2.5:1 Glucose:M molar ratio sample, which contained a La_2O_3 phase. For all other formulations, only very minor or no impurity peaks were detected in the XRD patterns. For samples processed at 1100 °C, a significant impurity, La_2SrO_x, occurred for 2.5:1 and 3.0:1 Glucose:M molar ratio formulations. Higher glucose concentrations, and, in turn, higher carbon template concentrations resulted in the formation of a pure LSCF phase. For all samples processed at 1200 °C, La_2O_3 was the primary phase detected. The La_2O_3 peaks were sharp, indicating large crystallites, and suggesting solid-state diffusion may have limited the ability to form the desired LSCF phase. This point is addressed in more detail later.

Figure 2 shows XRD patterns of LSCF-POG treated in argon and subsequently calcined in air for samples with Glucose:M molar ratios of 2.5:1, 3.5:1, and 4.5:1. Similar to samples processed in nitrogen, the primary peaks correspond to La_2O_3 and FeCo and peak broadness increases with increasing Glucose:M molar ratio and decreasing processing temperature. SrO appears as a minor phase in the 3.5:1 Glucose:M sample, Fig. 2b; however, SrO does not appear in the 2.5:1 and 4.5:1 samples. This suggests that the formation of a crystalline SrO phase may be specific to the carbon template concentration, not having formed above and below the 3.5:1 Glucose:M concentration. More importantly, there is no indication

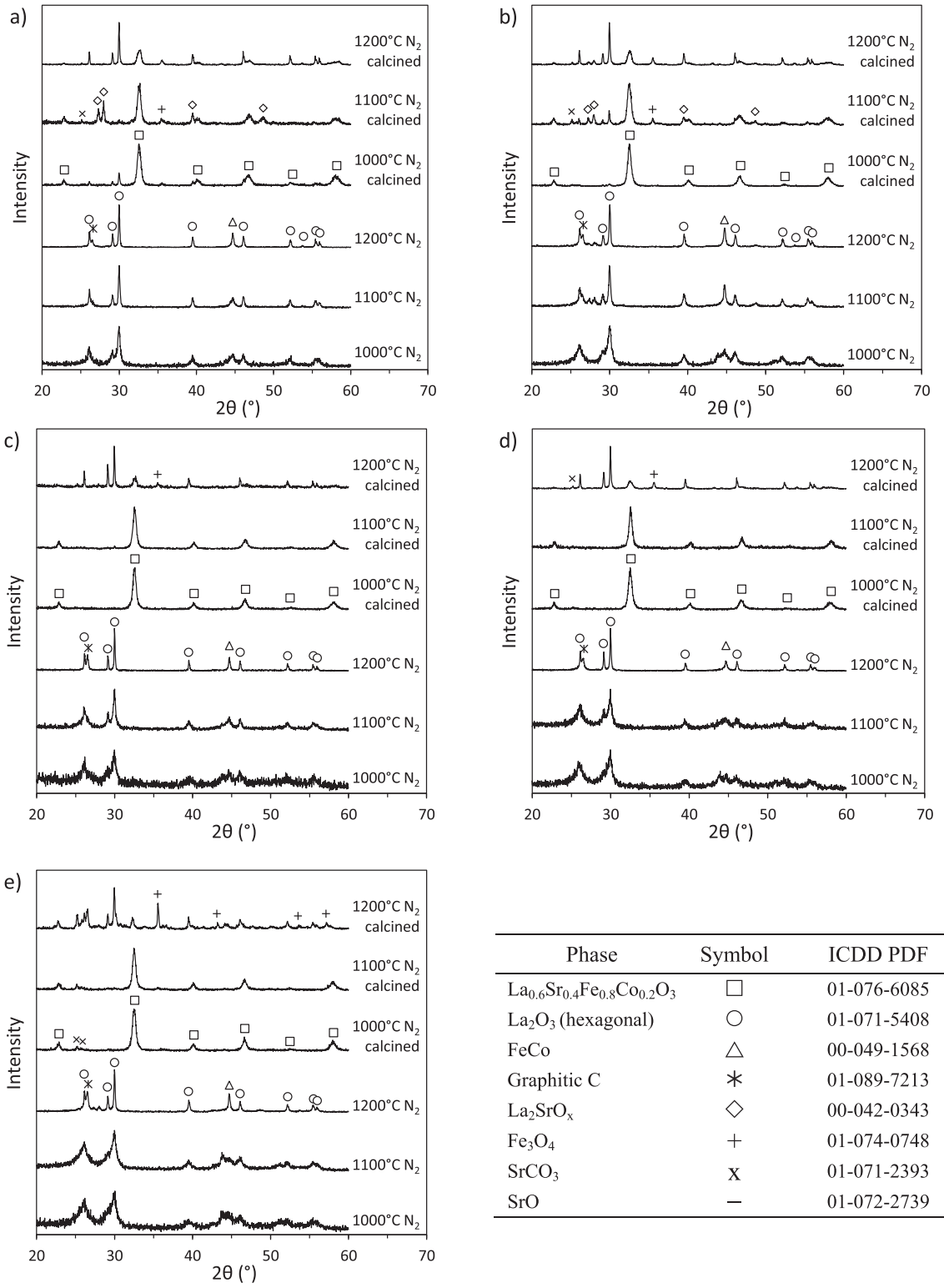

Phase	Symbol	ICDD PDF
$La_{0.6}Sr_{0.4}Fe_{0.8}Co_{0.2}O_3$	□	01-076-6085
La_2O_3 (hexagonal)	○	01-071-5408
FeCo	△	00-049-1568
Graphitic C	✳	01-089-7213
La_2SrO_x	◇	00-042-0343
Fe_3O_4	+	01-074-0748
$SrCO_3$	x	01-071-2393
SrO	–	01-072-2739

Figure 1. X-ray diffraction patterns of LSCF-POG with varying Glucose:M molar ratio after heating in nitrogen and after calcining in air at 700 °C. Glucose:M ratios are (a) 2.5:1, (b) 3.0:1, (c) 3.5:1, (d) 4.0:1, and (e) 4.5:1. The ICDD phase key applies to Figs. 1, 2, and 5.

of a graphitic carbon peak over the range of sample formulations and processing temperatures studied, suggesting that the carbon template generated in situ is amorphous. This result is consistent with a previous report that graphitic carbon forms upon heating glucose in a nitrogen atmosphere, but remains amorphous when heated in a helium atmosphere.[36] In addition to the lack of a graphitic carbon peak upon processing in argon, the peaks are consistently broader compared to processing in nitrogen. Upon calcination, Fig. 2 shows that the desired LSCF phase forms with a very minor strontium carbonate impurity for all samples, demonstrating a stark difference between processing atmospheres. LSCF forms more readily in an argon processing atmosphere compared to nitrogen.

Regarding the differences in graphitization between nitrogen and helium previously reported by Barbera et al., it was argued that

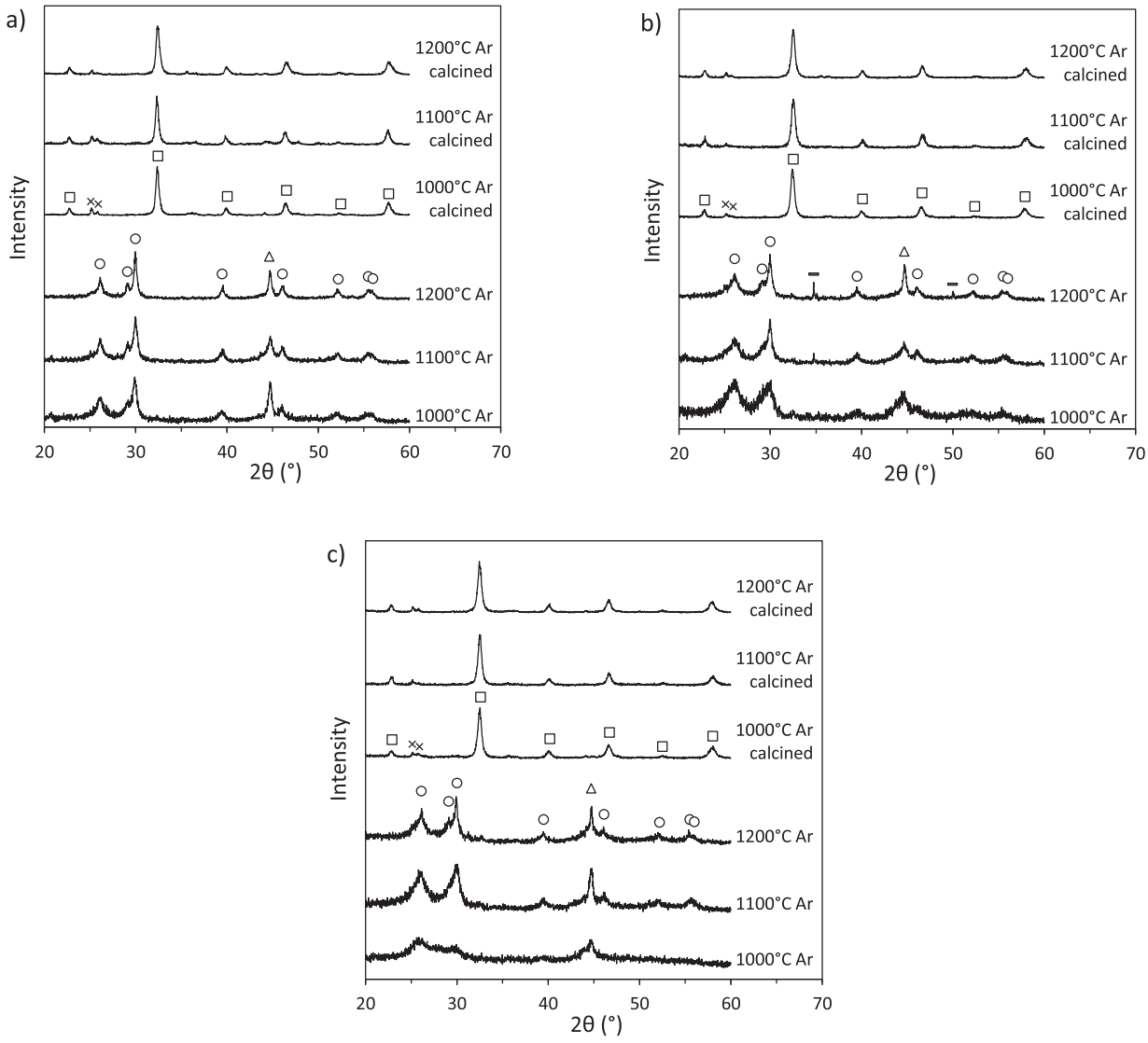

Figure 2. X-ray diffraction patterns of LSCF-POG with varying Glucose:M molar ratio after heating in argon and followed by calcining in air at 700 °C. Glucose:M ratios are (a) 2.5:1, (b) 3.5:1, and (c) 4.5:1. Phase legend is located in Fig. 1.

oxygen functional groups form on the carbon surface upon heating in nitrogen, which was found to not occur in helium, and those oxygen species catalyze the graphitization process.[36] A 99.99% pure nitrogen stream was used in that study and the authors proposed that small traces of oxygen in the nitrogen stream preserved the oxygen species on the carbon surface. The nitrogen purity in this study was 99.997% with an oxygen impurity concentration <10 ppm and the argon purity was 99.998% with an oxygen impurity concentration of <5 ppm. Even though our nitrogen gas had a higher purity, we processed a LSCF hybrid material with a 3.5:1 Glucose:M concentration at 1200 °C in ultra-high purity nitrogen, 99.999% purity and an oxygen concentration <1 ppm, to explore the effect of oxygen impurity concentration. In this case, a significant La_2O_3 impurity phase still formed upon calcination in air. The relative peak intensity of the La_2O_3 phase was not as strong as the 99.997% nitrogen; however, the impurity was significant and a pure LSCF phase did not form as was observed when processed in argon. Given this result, we suggest that although oxygen concentration may play a role in the graphitization process, there are likely other factors causing the different LSCF results in nitrogen and argon that are not understood at this time.

In comparing XRD patterns of processed samples prior to calcination in Figs. 1 and 2, it is clear that the La_2O_3 peaks are broader for samples processed in argon compared to nitrogen. Furthermore, broader XRD peaks correspond to smaller crystallite sizes. Thus, one would expect that smaller La_2O_3 crystallites in argon processed samples result in shorter solid-state diffusion paths to form LSCF during calcination. Conversely, nitrogen processed samples do not form LSCF upon calcination due to diffusion limitations, with larger La_2O_3 crystallites requiring longer diffusion paths. To better understand links between crystallite size and successfully forming the desired LSCF phase, La_2O_3 crystallite sizes were estimated using the Scherrer equation for all processed samples prior to calcination, Fig. 3. As shown in Fig. 3a, La_2O_3 crystallite size decreased with increasing carbon template concentration and decreasing processing temperature for samples processed in nitrogen. Crystallite size ranged between 39 nm and 9 nm over the range of sample formulations and processing temperatures studied. The La_2O_3 crystallite size of argon processed samples also decreased with increasing carbon template concentration and decreasing processing temperature; however, the range of crystallite sizes was smaller, only spanning 17 nm to 10 nm (Fig. 3b).

In comparing conditions that resulted in the desired LSCF phase to La_2O_3 crystallite size, a trend becomes clear, indicated in Fig. 3. If the processed sample had a La_2O_3 crystallite size above 20 nm, then significant impurities were present upon calcination. If the crystallite

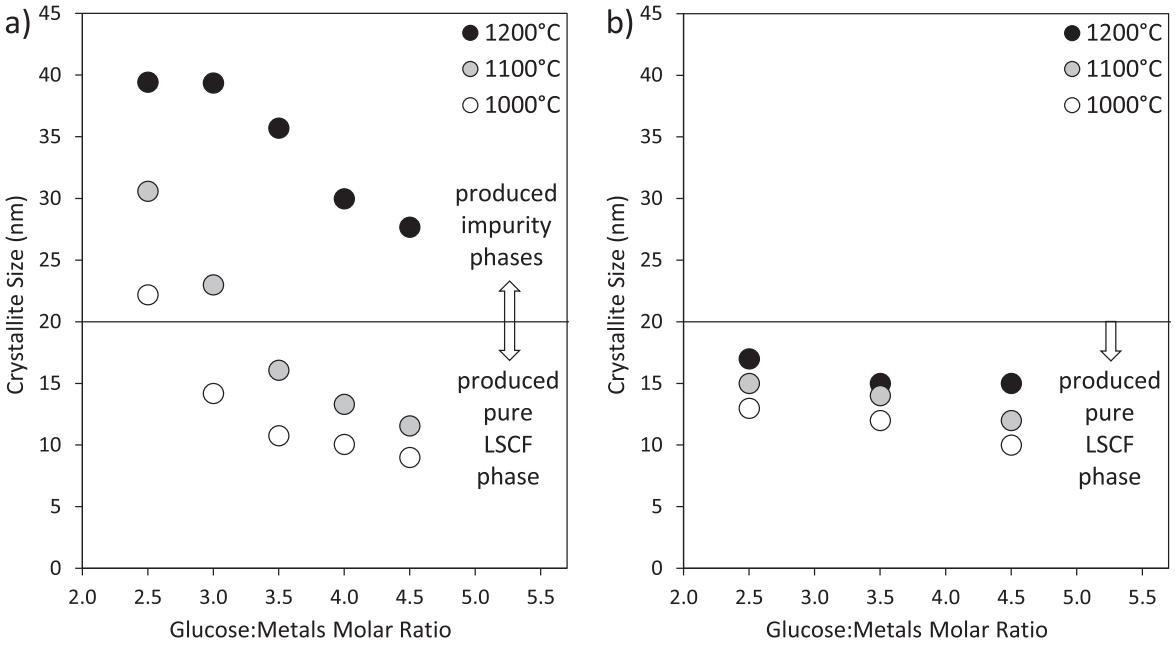

Figure 3. La_2O_3 crystallite size in LSCF-POG samples as a function of Glucose:M molar ratio after heating to various temperatures in (a) nitrogen and (b) argon.

size was below 20 nm, LSCF was the primary phase with very minor or no impurities upon calcination. This trend suggests that La_2O_3 crystallite size is the limiting factor in producing the desired LSCF phase. TEM images, shown in Fig. 4, support the crystallite size analysis. For a 2.5:1 Glucose:M LSCF-POG sample processed in nitrogen at 1200 °C, the La_2O_3 characteristic particle size is about 240 nm, Fig. 4a. For the same sample processed in argon, the La_2O_3 characteristic particle size is about 40 nm, Fig. 4b. Similar trends are observed for FeCo particles. The FeCo characteristic particle size is about 150 nm in nitrogen and 30 nm in argon.

Elemental analysis of the La_2O_3 particles, Fig. 4e, indicates that the A-site comprises a mixture of lanthanum and strontium, which is consistent with the absence of a strontium-specific phase in the XRD patterns shown in Figs. 1 and 2 for a 2.5:1 Glucose:M sample processed at 1200 °C. The La–Sr–O particles are slightly lanthanum-rich, with a La:Sr stochiometry of ∼70:30 whereas the La:Sr precursor stoichiometry was 60:40. Some strontium was detected in carbon-rich particles, e.g. point three in Fig. 4a, which could account for the slightly lower strontium content in the La–Sr–O particles. The FeCo stoichiometry in Figs. 4a and 4b more closely align with the precursor stoichiometry, 85:15 and 79:21 compared to 80:20.

To better understand differences in the carbon template of samples processed in nitrogen and argon, carbon elemental analysis and surface area measurements were conducted, Table I. For all samples, regardless of being processed in nitrogen or argon, the carbon template concentration was essentially the same, ranging between 45–48 wt%. Significant differences, however, were observed in the specific surface area of samples processed in nitrogen versus argon. Samples processed in nitrogen consistently had a lower specific surface area. For example, the surface area of samples processed at 1200 °C were 22 $m^2 \cdot g^{-1}$ and 54 $m^2 \cdot g^{-1}$ for nitrogen and argon, respectively. It is important to note that the surface area is an overall value for mixtures of La–Sr–O, FeCo, and carbon particles. Using the particle sizes observed with TEM imaging, Fig. 4, one can estimate the surface area contributions of each mixture component. For a sample of 2.5:1 Glucose:M LSCF-POG processed in nitrogen at 1200 °C, and assuming spherical particles of equal size, the La–Sr–O and FeCo surface areas are estimated to be approximately 4 $m^2 \cdot g^{-1}$ and 5 $m^2 \cdot g^{-1}$, respectively Assuming equal amounts of La–Sr–O and FeCo by weight and using the carbon wt% shown in Table I, the carbon template specific surface area is estimated to be ∼40 $m^2 \cdot g^{-1}$. Using similar calculations for the 2.5:1 sample processed in argon at 1200 °C, the carbon template specific surface area is estimated to be ∼90 $m^2 \cdot g^{-1}$. Here we propose that the specific surface area of the carbon template in nitrogen processed samples is lower because some portion of the carbon template comprised graphitic carbon, whereas the carbon template in argon processed samples was amorphous. Indeed, amorphous carbon has been reported to have higher specific surface areas than graphitic carbon.[37] Importantly, the carbon template specific surface area corresponds to the La–Sr–O and FeCo specific surface areas; a higher carbon template surface area results in smaller La–Sr–O and FeCo particles.

Upon calcination of the 2.5:1 Glucose:M sample processed in nitrogen at 1200 °C, TEM imaging and elemental analysis, Figs. 4c and 4e, indicate that most of the strontium in the La–Sr–O phase has diffused into a strontium-rich LSCF phase, leaving behind La_2O_3 particles with a characterisitic size of ∼150 nm. The strontium-rich LSCF phase is of order 10 nm in size. In addition, an iron oxide phase with a particle size of order 10 nm was detected. In comparison, the same sample processed in argon and then calcined in air was found to have LSCF particles with a more balanced stoichiometry of La and Sr and a characteristic size of 30–40 nm. Fe–Co–O particles were also detected with a characteristic size of order 10 nm, which corresponds to a minor peak in Fig. 2a that matches a Fe_3O_4 standard XRD pattern.

Table II shows the final specific surface area of LSCF samples calcined at 700 °C. Overall, the specific surface area of samples sintered in argon and nitrogen were similar, all between the range of 20–29 $m^2 \cdot g^{-1}$, regardless of the Glucose:M molar ratio and processing temperature. It is likely that the LSCF particles converged on the 20–29 $m^2 \cdot g^{-1}$ range because the carbon template oxidizes at 550 °C,[20] leaving no template in the samples between 550 °C and 700 °C. For comparison, the specific surface area of a 4.5:1 Glucose:M sample directly sintered in air is also shown in Table II. Directly sintering in air at 1000 °C, 1100 °C, and 1200 °C resulted in LSCF surface areas of 2.5 $m^2 \cdot g^{-1}$, 0.9 $m^2 \cdot g^{-1}$, and 0.3 $m^2 \cdot g^{-1}$, respectively, which is about 10, 30, and 80 times lower than LSCF-POG samples processed in an inert atmosphere. Furthermore, the specific surface areas of commercial LSCF particles heated in air at 1000 °C, 1100 °C, and 1200 °C were 2.1 $m^2 \cdot g^{-1}$, 1.2 $m^2 \cdot g^{-1}$, and

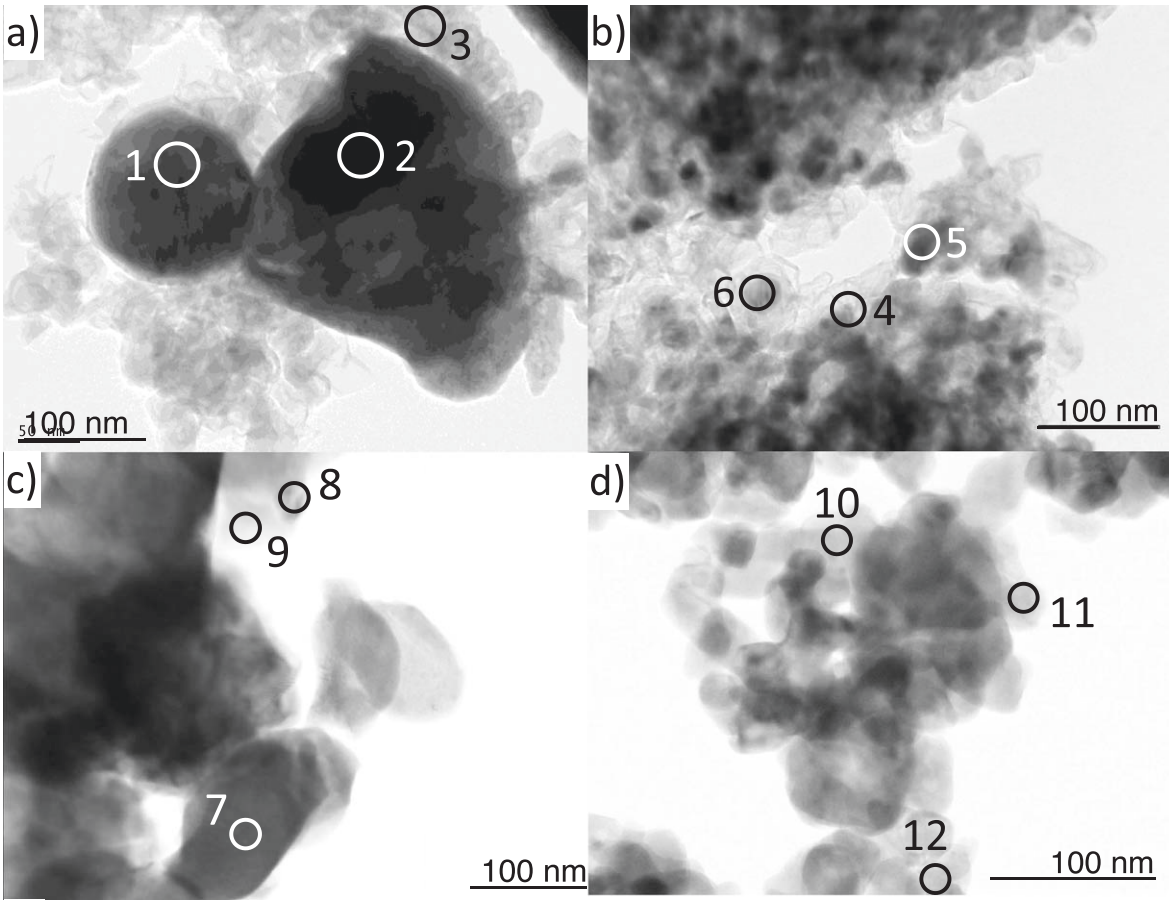

e)

	1	2	3	4	5	6	7	8	9	10	11	12
La		15.8		22.6	17.6		22.5		3.9	6.9		9.0
Sr		7.5	2.7	7.3	8.1				9.4	6.3		4.0
Co	15					21	0.3		1.6	2.4	2.5	2.6
Fe	85					79		10.6	10.9	9.8	10.8	12.0
O		76.7		70.1	74.3		77.2	89.4	74.2	74.6	86.7	72.4
C			91.3									

Figure 4. TEM images of LSCF-POG with a Glucose:M molar ratio of 2.5:1 after heating to (a) 1200 °C in nitrogen, (b) 1200 °C in argon, (c) 1200 °C in nitrogen followed by 700 °C in air, and (d) 1200 °C in argon followed by 700 °C in air. (e) EDS chemical composition in atomic percentage.

Table I. Carbon content and specific surface area of LSCF-POG with a 2.5:1 Glucose:M molar ratio after heating to various temperatures in nitrogen and argon.

T (°C)	1000		1100		1200	
Gas	N_2	Ar	N_2	Ar	N_2	Ar
Carbon (wt%)	47	46	45	48	47	46
Surface area ($m^2 \cdot g^{-1}$)	44	77	47	62	22	54

0.2 $m^2 \cdot g^{-1}$, respectively. This stark difference demonstrates the utility of the in situ carbon templating method in generating high surface area LSCF at traditional sintering temperatures.

All of the results presented thus far were for samples calcined in air at 700 °C. It is expected that increasing the calcination temperature will eventually result in a pure LSCF phase for nitrogen processed samples. To explore the effect of calcination temperature, XRD patterns were collected between 700 °C–900 °C for a 2.5:1 Glucose:M LSCF-POG sample processed in nitrogen at 1100 °C, Fig. 5. At 750 °C the La_2SrO_x is no longer detected and a La_2O_3 phase forms. The La_2O_3 peak intensity lessens with increasing temperature, and a La_2O_3 phase is no longer present after heating to 900 °C. After calcination at 900 °C, the LSCF specific surface area was 6 $m^2 \cdot g^{-1}$. This surface area falls within the expected range given the surface areas measured for samples calcined at 700 °C (~25 $m^2 \cdot g^{-1}$) and directly sintered in air at 1000 °C (~2 $m^2 \cdot g^{-1}$).

Finally, the electrochemical behavior of symmetrical cells comprising nLSCF electrodes and cLSCF electrodes were compared, Fig. 6. The Nyquist plots in Fig. 6a indicate that the nLSCF cell had a higher ohmic impedance than the cLSCF cell. The theoretical ohmic contribution from the SDC electrolyte is expected to be 0.69 $\Omega \cdot cm^2$ at 700 °C, 0.48 $\Omega \cdot cm^2$ at 750 °C, and 0.35 $\Omega \cdot cm^2$ at 800 °C.[38] It should be noted that these values represent the total electrolyte ohmic resistance divided by two. This was done to make it easier to compare the electrolyte ohmic contributions to Fig. 6a because, as described in the Experimental section, the symmetric cell impedance spectra were divided by two. The calculated SDC ohmic contributions are essentially identical to the total ohmic resistances of the

Table II. LSCF specific surface area after heating LSCF-POG samples to various temperatures in nitrogen and argon followed by calcining in air at 700 °C. For comparison, some samples were heated directly in air. "x" indicates that a value was not reported due to the sample containing significant impurity phases.

T °C)	Gas	Glucose:Metals Molar Ratio				
		2.5:1	3.0:1	3.5:1	4.0:1	4.5:1
1000	N_2	x	25	23	25	24
	Ar	20	24	24	26	25
	Air					2.5
1100	N_2	x	x	24	26	24
	Ar	23	27	24	25	29
	Air					0.9
1200	N_2	x	x	x	x	x
	Ar	21	22	22	25	24
	Air					0.3

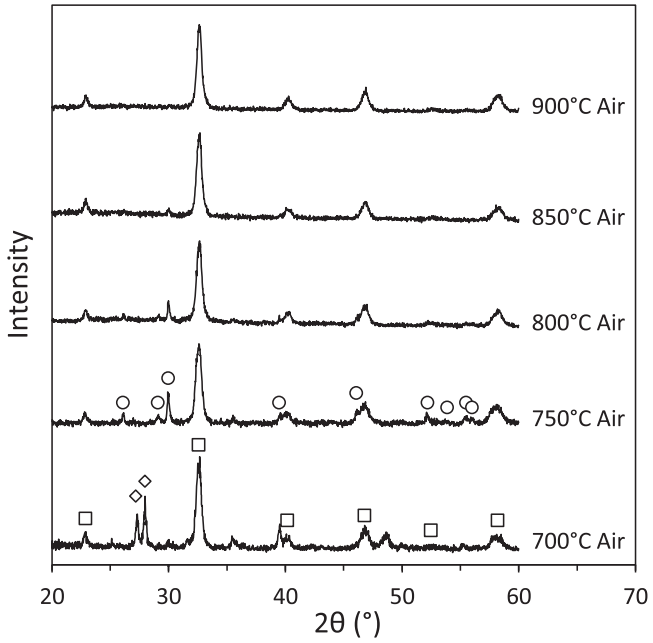

Figure 5. X-ray diffraction patterns of LSCF-POG with a 2.5:1 Glucose:M molar ratio after heating in nitrogen to 1100 °C followed by calcining in air at varying temperatures. Phase legend is located in Fig. 1.

cLSCF cell, suggesting that the ohmic resistance within the LSCF electrode is negligible. This is reasonable given that the electronic conductivity of a porous LSCF electrode is of order 10^2 S·cm^{-1} and the theoretical ohmic resistance would be of order 10^{-4} Ω·cm^2.[38,39] In addition, any ohmic contributions due to interfacial resistance of oxygen ion transport between the electrode and electrolyte appears to be negligible for the cLSCF cell because the ohmic resistance matches that of the SDC electrolyte.

Compared to the cLSCF cell, the ohmic resistance of the nLSCF cell tells a different story. Subtracting the ohmic contribution of the SDC electrolyte from the nLSCF cell, the remaining ohmic resistance to be accounted for is 0.37 Ω·cm^2 at 700 °C, 0.23 Ω·cm^2 at 750 °C, and 0.16 Ω·cm^2 at 800 °C. Clearly, there is a significant contribution to the total ohmic resistance with the nLSCF cell that is not observed with the cLSCF cell. Two possible explanations for the additional resistance are poor conductivity within the LSCF electrode and poor oxygen ion transport between the electrode and electrolyte. If the additional ohmic resistance was due to poor conductivity within the nLSCF electrodes, the corresponding electrode electronic conductivities would be of order 10^{-3} S·cm^{-1}. This is six orders of magnitude lower than the bulk conductivity of LSCF. It is highly unlikely that the nLSCF conductivity would be six orders of magnitude lower than the bulk given that infiltrated networks of nanoparticles just above the percolation threshold have a conductivity that is about three orders of magnitude lower than the bulk.[39,40] Thus, it is more likely that the additional ohmic resistance is due to an interfacial resistance to oxygen ion transport between the electrode and electrolyte, which has been reported for electrode particles poorly connected to the electrolyte.[41,42]

To probe whether interfacial resistance dominates the impedance of the nLSCF cell, one can consider the polarization resistance and its characteristic frequencies. The polarization resistances are calculated by subtracting the high frequency intercept of the Nyquist plot, Fig. 6a, from the low frequency intercept. The polarization resistances were 0.34 Ω·cm^2 at 700 °C, 0.19 Ω·cm^2 at 750 °C, and 0.12 Ω·cm^2 at 800 °C for the cLSCF cell and 0.72 Ω·cm^2 at 700 °C, 0.35 Ω·cm^2 at 750 °C, and 0.20 Ω·cm^2 at 800 °C for the nLSCF cell. In all cases, the polarization resistance was higher for the nLSCF cell. This is not inconsistent with a significant nLSCF interfacial resistance because polarization resistance has been shown to increase with an increase in interfacial resistance between the electrode and electrolyte.[43] Bode plots in Figs. 6b–6c show the relationship between frequency and the imaginary component of the impedance for the cLSCF and nLSCF cells. The peak frequency for the cLSCF cell was between 10–20 Hz over the 700 °C–800 °C temperature range. The peak frequency for the nLSCF was much higher, 1–2 kHz. The literature typically attributes a peak frequency of 10–20 Hz to gas diffusion limitations through the electrode or current collector layer and a peak frequency of 1–2 kHz to oxygen ion transport limitations between the electrode and electrolyte.[41,42,44,45] To further support this explanation, the polarization resistances were measured as a function of partial pressure of oxygen, $P(O_2)$. Bode plots for a cLSCF cell and a nLSCF cell as a function of $P(O_2)$ are shown in Fig. S1 (available online at stacks.iop.org/JES/168/034519/mmedia). The cLSCF cell showed a strong $P(O_2)$ dependence, confirming that the impedance was dominated by gas diffusion limitations. The nLSCF cell showed a weak $P(O_2)$ dependence, further supporting that an interfacial resistance dominates the impedance.

Overall, the nLSCF cell results suggest a poor particle connection between the electrode and electrolyte. Although the poor connection resulted in a higher impedance than a traditional electrode, the results demonstrate that high surface area nanoparticles were preserved during the in situ carbon templating process when applied as electrodes on an electrolyte substrate. To improve the overall electrode impedance of a nLSCF cell, the interfacial resistance needs to be improved. One possible route is to lower the carbon template concentration. A beneficial feature of the in situ carbon templating process is that the carbon template concentration is directly related to the amount of glucose used in the formulation. Thus, lowering the glucose concentration would lower the carbon template concentration and likely form a better connection between the LSCF particles and the SDC electrolyte. Of course, by lowering the carbon template concentration, the LSCF surface area will likely decrease. Therefore, one would need to find a balance between lowering the interfacial resistance and maintaining an enhanced LSCF surface area. A more fruitful approach may be to prepare electrode composites of nLSCF with SDC particles. Indeed, GDC-LSCF composites have been shown to decrease polarization by a factor of ∼10 compared to LSCF electrodes.[42] Rather than forming porous composites with roughly equal size LSCF and SDC particles, our hybrid material approach is more likely to result in porous composites comprised of large SDC particles and LSCF nanoparticles. It is our hope that this unique approach may result in composite structures that more closely mimic infiltrated electrodes than traditionally co-sintered electrodes. Infiltrated electrodes often show significantly lower impedance compared to traditionally co-sintered electrodes due to

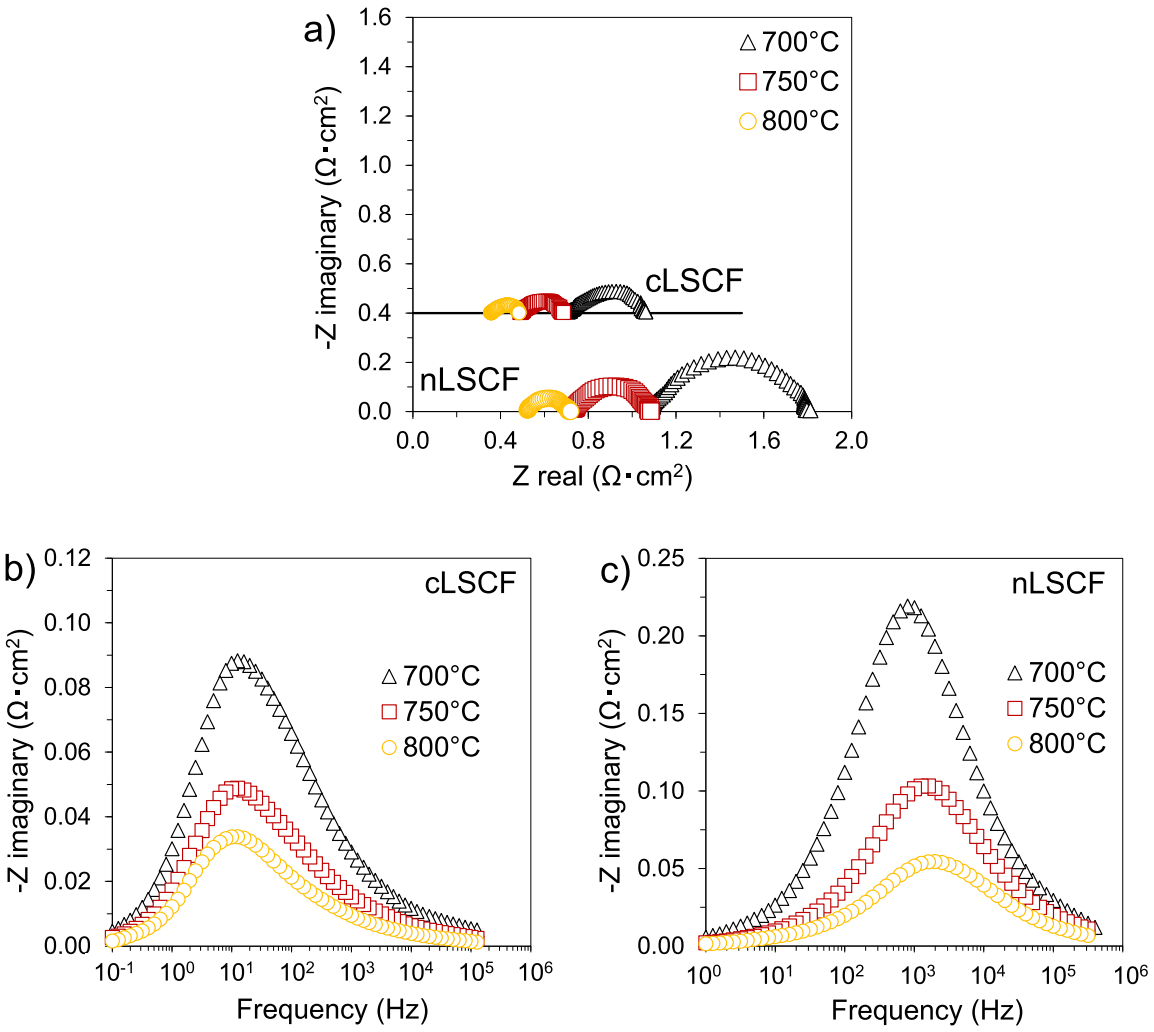

Figure 6. (a) Nyquist plots and (b)–(c) Bode plots of symmetric cells with nLSCF and cLSCF electrodes.

their unique structure;[46–49] however, fabricating infiltrated electrodes is difficult, requiring many infiltration and calcination steps. Our approach of co-sintering SDC particles with hybrid LSCF material may result in a structure closer to that of infiltrated electrodes, enhancing performance without the need for infiltration. We are currently exploring this approach.

Conclusions

The thermochemical stability of high surface area LSCF nanoparticles generated by the in situ carbon templating method was studied in two sintering atmospheres, nitrogen and argon. An amorphous carbon template formed for all samples processed in argon, however, graphitic carbon was observed upon processing in nitrogen. The presence of graphitic carbon corresponded to larger La_2O_3 crystallites, >20 nm, and resulted in a LSCF phase with significant impurities. Conversely, an amorphous carbon template corresponded to La_2O_3 crystallites <20 nm and resulted in a pure LSCF phase. The specific surface area of LSCF samples processed by in situ carbon templating was 10–80 times higher than samples processed conventionally in air. Electrochemical impedance demonstrated that nLSCF electrodes are limited by a high interfacial resistance, demonstrating that electrodes comprising LSCF nanoparticles were also produced on electrolyte substrates in the 1000 °C–1200 °C range.

Acknowledgments

This work was supported by the National Science Foundation Faculty Early Career Development (CAREER) award (CMMI-1651186) and the National Energy Technology Laboratory's ongoing research under the RSS Contract 89243318CFE000003. Helpful discussions with Harry Finklea (Department of Chemistry, West Virginia University) are gratefully acknowledged. We also thank Jian Liu (National Energy Technology Laboratory, Morgantown, WV) for assistance with $P(O_2)$ dependence measurements.

Disclaimer

This project was funded by the Department of Energy, National Energy Technology Laboratory, an agency of the United States Government, through a support contract with Leidos Research Support Team (LRST). Neither the United States Government nor any agency thereof, nor any of their employees, nor LRST, nor any of their employees, makes any warranty, expressed or implied, or assumes any legal liability or responsibility for the accuracy, completeness, or usefulness of any information, apparatus, product, or process disclosed, or represents that its use would not infringe privately owned rights. Reference herein to any specific commercial product, process, or service by trade name, trademark, manufacturer, or otherwise, does not necessarily constitute or imply its endorsement, recommendation, or favoring by the United States Government or any agency thereof. The views and opinions of

authors expressed herein do not necessarily state or reflect those of the United States Government or any agency thereof.

ORCID

Sixbert P. Muhoza https://orcid.org/0000-0002-9986-4241
Michael D. Gross https://orcid.org/0000-0002-2280-2034

References

1. S. P. Jiang, *Solid State Ion.*, **146**, 1 (2002).
2. A. Esquirol, N. P. Brandon, J. A. Kilner, and M. Mogensen, *J. Electrochem. Soc.*, **151**, A1847 (2004).
3. F. S. Baumann, J. Fleig, H. U. Habermeier, and J. Maier, *Solid State Ion.*, **177**, 1071 (2006).
4. D. Marinha, L. Dessemond, J. S. Cronin, J. R. Wilson, S. A. Barnett, and E. Djurado, *Chem. Mater.*, **23**, 5340 (2011).
5. S. P. Jiang, *Int. J. Hydrog. Energy*, **44**, 7448 (2019).
6. Y. Teraoka, H. M. Zhang, K. Okamoto, and N. Yamazoe, *Mater. Res. Bull.*, **23**, 51 (1988).
7. S. Carter, A. Selcuk, R. J. Charter, J. Kajda, J. A. Kilner, and B. C. H. Steele, *Solid State Ion.*, **53-6**, 597 (1992).
8. M. Katsuki, S. Wang, M. Dokiya, and T. Hashimoto, *Solid State Ion.*, **156**, 453 (2003).
9. S. Zongping, Z. Wei, and Z. Zhonghua, *Prog. Mater. Sci.*, **57**, 804 (2012).
10. K. Q. Huang, R. Tichy, and J. B. Goodenough, *J. Am. Ceram. Soc.*, **81**, 2581 (1998).
11. S. P. Jiang, *J. Power Sources*, **124**, 390 (2003).
12. N. P. Bansal and Z. M. Zhong, *J. Power Sources*, **158**, 148 (2006).
13. Y. P. Fu, S. B. Wen, and C. H. Lu, *J. Am. Ceram. Soc.*, **91**, 127 (2008).
14. S. Celerier, C. Laberty, F. Ansart, P. Lenormand, and P. Stevens, *Ceram. Int.*, **32**, 271 (2006).
15. J. X. Wang, Y. K. Tao, J. Shao, and W. G. Wang, *J. Power Sources*, **186**, 344 (2009).
16. Y. Leng, S. H. Chan, and Q. Liu, *Int. J. Hydrog. Energy*, **33**, 3808 (2008).
17. Q. Xu, D. Huang, W. Chen, J. Lee, H. Wang, and R. Yuan, *Scr. Mater.*, **50**, 165 (2004).
18. M. R. Cesario, D. A. Macedo, A. E. Martinelli, R. M. Nascimento, B. S. Barros, and D. M. A. Melo, *Cryst. Res. Technol.*, **47**, 723 (2012).
19. A. Dutta, J. Mukhopadhyay, and R. N. Basu, *J. Eur. Ceram. Soc.*, **29**, 2003 (2009).
20. M. Cottam, S. Muhoza, and M. D. Gross, *J. Am. Ceram. Soc.*, **99**, 2625 (2016).
21. S. P. Muhoza, M. A. Cottam, and M. D. Gross, *J. Vis. Exp.*, **122**, e55500 (2017).
22. S. P. Muhoza, T. E. Barrett, S. E. Soll, and M. D. Gross, *ECS Trans.*, **78**, 1407 (2017).
23. S. P. Muhoza, T. E. Barrett, M. A. Cottam, S. E. Soll, M. D. Yuce, V. S. Prathab, S. K. Hambright, M. Rezazad, O. Racchi, and M. D. Gross, *J. Electrochem. Soc.*, **165**, F46 (2018).
24. S. P. Muhoza, A. McCormack, R. W. Garrett, M. D. Yuce, V. S. Prathab, S. K. Hambright, M. A. Cottam, and M. D. Gross, *J. Electrochem. Soc.*, **166**, F53 (2019).
25. S. P. Muhoza, S. Lee, X. Song, B. Guan, T. Yang, and M. D. Gross, *J. Electrochem. Soc.*, **167**, 024517 (2020).
26. S. R. Shatynski, *Oxid. Met.*, **13**, 105 (1979).
27. A. Maitre and P. Lefort, *Solid State Ion.*, **104**, 109 (1997).
28. D. R. Gaskell, *Introduction to the Thermodynamics of Materials* (Taylor & Francis, New York) 4th ed., p. 429 (2003).
29. T. J. Chung, H. Song, G. H. Kim, and D. Y. Kim, *J. Am. Ceram. Soc.*, **80**, 2607 (1997).
30. Y. K. Paek, J. H. Ahn, G. H. Kim, and S. J. L. Kang, *J. Am. Ceram. Soc.*, **85**, 1631 (2002).
31. A. Diaz-Parralejo, A. L. Ortiz, F. Rodriguez-Rojas, and F. Guiberteau, *Thin Solid Films*, **518**, 2779 (2010).
32. M. Lerch, *J. Am. Ceram. Soc.*, **79**, 2641 (1996).
33. L.-W. Tai, M. M. Nasrallah, and H. U. Anderson, *J. Solid State Chem.*, **118**, 117 (1995).
34. D. Udomsilp, D. Roehrens, N. H. Menzler, A. K. Opitz, O. Guillon, and M. Bram, *Mater. Lett.*, **192**, 173 (2017).
35. L. Zhu, B. Wei, Y. Zhang, Z. Lü, Z. Wang, X. Huang, Z. Cao, W. Jiang, and Y. Li, *Electrochim. Acta*, **160**, 89 (2015).
36. K. Barbera, L. Frusteri, G. Italiano, L. Spadaro, F. Frusteri, S. Perathoner, and G. Centi, *Chinese J. Catal.*, **35**, 869 (2014).
37. O. N. Shornikova, E. V. Kogan, N. E. Sorokina, and V. V. Avdeev, *Russ. J. Phys. Chem. A*, **83**, 1022 (2009).
38. Q. Xu, D.-P. Huang, F. Zhang, W. Chen, M. Chen, and H.-X. Liu, *J. Alloys Comp.*, **454**, 460 (2008).
39. M. J. Synodis, C. L. Porter, N. M. Vo, A. J. L. Reszka, M. D. Gross, and R. C. Snyder, *J. Electrochem. Soc.*, **160**, F1216 (2013).
40. A. J. L. Reszka, R. C. Snyder, and M. D. Gross, *J. Electrochem. Soc.*, **161**, F1176 (2014).
41. V. Dusastre and J. A. Kilner, *Solid State Ionics*, **126**, 163 (1999).
42. E. P. Murray, M. J. Sever, and S. A. Barnett, *Solid State Ionics*, **148**, 27 (2002).
43. T. Kenjo and Y. Kanehira, *Solid State Ionics*, **148**, 1 (2002).
44. Y. Chen et al., *Adv. Energy Mater.*, **7**, 1601890 (2017).
45. H. Xu, H. Zhang, and A. Chu, *Int. J. Hydrog. Energy*, **41**, 22415 (2016).
46. J. M. Vohs and R. J. Gorte, *Adv. Mater.*, **21**, 943 (2009).
47. Z. Jiang, C. Xia, and F. Chen, *Electrochim. Acta*, **55**, 3595 (2010).
48. C. Yang, C. Jin, A. Coffin, and F. Chen, *Int. J. Hydrog. Energy*, **35**, 5187 (2010).
49. Y. Huang, J. M. Vohs, and R. J. Gorte, *J. Electrochem. Soc.*, **151**, A646 (2004).